Tuning spin-charge interconversion with quantum confinement in ultrathin bismuth films

C. Zucchetti,[1] M.-T. Dau,[2] F. Bottegoni,[1] C. Vergnaud,[2] T. Guillet,[2] A. Marty,[2] C. Beigné,[2] S. Gambarelli,[3] A. Picone,[1] A. Calloni,[1] G. Bussetti,[1] A. Brambilla,[1] L. Duò,[1] F. Ciccacci,[1] P. K. Das,[4] J. Fujii,[4] I. Vobornik,[4] M. Finazzi,[1] and M. Jamet[2,*]

[1]*LNESS-Dipartimento di Fisica, Politecnico di Milano, Piazza Leonardo da Vinci 32, 20133 Milano, Italy*
[2]*Univ. Grenoble Alpes, CEA, CNRS, Grenoble INP (Institute of Engineering Univ. Grenoble Alpes), INAC-Spintec, 38000 Grenoble, France*
[3]*Univ. Grenoble Alpes, CEA, INAC-SYMMES, 38000 Grenoble, France*
[4]*CNR-IOM Laboratorio TASC, 34149 Trieste, Italy*

Spin-charge interconversion (SCI) phenomena have attracted a growing interest in the field of spintronics as a means to detect spin currents or manipulate the magnetization of ferromagnets. The key ingredients to exploit these assets are a large conversion efficiency, the scalability down to the nanometer scale, and the integrability with optoelectronic and spintronic devices. Here, we show that, when an ultrathin Bi film is epitaxially grown on a Ge(111) substrate, quantum size effects arising in nanometric Bi islands drastically boost the SCI efficiency, even at room temperature. Using x-ray diffraction, scanning tunneling microscopy, and spin- and angle-resolved photoemission, we obtain a clear picture of the film morphology, crystal, and electronic structures. We then directly probe SCI with three different techniques: magneto-optical Kerr effect to detect the charge-to-spin conversion generated by the Rashba-Edelstein effect (REE), optical spin orientation, and spin pumping to generate spin currents and measure the spin-to-charge conversion generated by the inverse Rashba-Edelstein effect (IREE). The three techniques show a sizable SCI only for 1–3-nm-thick Bi films corresponding to the presence of bismuth nanocrystals at the surface of germanium. Due to three-dimensional quantum confinement, those nanocrystals exhibit a highly resistive volume separating metallic surfaces where SCI takes place by (I)REE. As the film size increases, the Bi film becomes continuous and semimetallic leading to the cancellation of SCIs occurring at opposite surfaces, resulting in an average SCI that progressively decreases and disappears. These results pave the way for the exploitation of quantum size effects in spintronics.

I. INTRODUCTION

Bismuth exhibits a series of remarkable electronic properties that have stimulated experimental and theoretical investigations for decades, in particular in electronic transport studies [1–3]. The lattice structure of Bi single layer films resembles that of graphene, while the electronic structure is endowed with a very large spin-orbit coupling of the order of 1.8 eV, which may give origin to topological states [4] or to surface states with a giant Rashba spin-orbit splitting [5] ranging from 0.5 eV [6] to 0.8 eV [7]. Bulk Bi has a rhombohedral crystal structure and is a semimetal with a very small indirect band overlap ($\approx$38 meV), resulting in a low charge carrier density compared with conventional metals. Electrons exhibit a long Fermi wavelength (λ_F) of 40 to 70 nm [8,9], which is more than one order of magnitude larger than in typical metals. Moreover, the electron effective mass m^* in bismuth amounts to $(0.001–0.26) m_e$, depending on the crystalline orientation, with m_e being the free electron mass [10]. The small m^* value combined with the long Fermi wavelength facilitates the observation of quantum size effects (QSE) which can drive semimetal to semiconductor (SMSC) transitions in low-dimensional systems [11].

To date, the spin properties of Bi films (spin diffusion length l_{sf} and spin Hall angle θ_{SH}) have shown a large dispersion in experimental values which is probably due to the crystalline state of the material. In amorphous Bi, Emoto *et al.* found: $l_{sf} = 8$ nm and $\theta_{SH} = 0.02$ [12] whereas, in polycrystalline Bi films, very different values were obtained: $l_{sf} = 0.11$ nm [13], 2.1 nm [14], 16 nm [15], 20 nm [16], or 50 nm [17] at room temperature up to 70 μm at 2 K [18] and $\theta_{SH} = 0.00012$ [16], 0.008 [19], 0.016 [15], 0.019 [17]. Despite the large spin-orbit coupling of Bi, the spin diffusion length is long and the spin-Hall angle ϑ_{SH} quite small, which is detrimental for SCI phenomena or spin-orbit torque switching. For these reasons, much effort has been devoted to the study of Bi-based systems in the ultrathin film limit, where several phenomena were observed such as allotropic transformations [20], the emergence of topologically protected [21] or superconducting [22] surface states, and SMSC transition [23], which may give rise to a very rich spin physics.

To investigate the thickness-dependent spin transport in this system, we have grown by molecular beam epitaxy (MBE) ultrathin Bi films ($t \approx 0$–10 nm) on Ge(111), after the deposition on the substrate of a Bi/Ge($\sqrt{3} \times \sqrt{3}$) R 30° wetting layer. The growth procedures for the various samples and the experimental details of the techniques used in this work are given in Sec. II. In Sec. III, we report the structural properties of thin Bi films on Ge(111) by means of scanning tunneling microscopy (STM). Electronic properties have been

*matthieu.jamet@cea.fr

studied by means of angle-resolved photoemission spectroscopy (ARPES) and spin-resolved ARPES (S-ARPES), at the APE beamline of ELETTRA (Sec. IV). The results of SCI which has been directly probed with magneto-optical Kerr effect (charge-to-spin conversion), or optical and electrical spin-injection (spin-to-charge conversion) are reported in Sec. V. The results are discussed in Sec. VI. We find negligible SCI except in a very narrow Bi thickness range corresponding to the existence of pseudocubic Bi nanocrystals in which QSE controls the spin transport. For small enough Bi nanocrystals, quantum confinement in all three spatial directions takes place and their volume becomes highly resistive in between metallic surfaces with strong Rashba spin-orbit interaction. From an electronic point of view, this situation is similar to a semimetal to semiconductor phase transition in Bi nanocrystals. For SCI, Bi nanocrystals behave the same as three-dimensional topological insulator thin films. These results pave the way for the exploitation of QSE in semimetals to tune SCI and open a route to manipulate spin currents in Ge by Rashba effect at the interface with a metal [24].

II. METHODS

ARPES and STM measurements were performed *in-situ* for bismuth thicknesses ranging from 0 to 10 nm. Bismuth was grown by molecular beam epitaxy on Ge(111) under ultrahigh vacuum (10^{-10} mbar), at room temperature and a deposition rate of 0.5 Å/s. The wetting layer was the Bi/Ge(111)-($\sqrt{3} \times \sqrt{3}$) R 30° surface obtained by depositing 1 ML of bismuth on Ge(111)-(2×2) annealed at 500 °C for 10 minutes [25,26]. 0–10 nm Bi wedges for optical and electrical measurements were grown in the same way. The Bi wedges for optical studies were protected by a ZrO$_2$(10 nm)/MgO(5 nm) bilayer grown *in situ*. The first nanometer of MgO was deposited using e-beam evaporation at a very low rate (0.025 Å/s) in order to limit the oxygen pressure in the MBE chamber and avoid partial oxidation of the Bi film. The last four nanometers were deposited at a rate of 0.25 Å/s. The ZrO$_2$ layer is grown *in situ* by RF sputtering. For spin pumping experiments, we deposited *in situ* an Al(5 nm)/Co(15 nm)/Al(3 nm) trilayer.

(S-)ARPES measurements were performed using *p*-polarized synchrotron radiation at the APE beamline of Elettra with a photon energy $h\nu = 50$ eV. The hemispherical electron energy and momentum analyzer (Scienta DA30) is equipped with two very low-energy electron diffraction (V-LEED)-based spin polarimeters. We probe the in-plane components of the spin polarization, and the spin-detection efficiency was corrected using a Sherman function ($S = 0.3$), determined by comparison with the known spin polarization of the Rashba-split surface states measured on the Au(111) surface. The spin polarization P is extracted as: $P = [I^+ - I^-]/[S \times (I^+ + I^-)]$, where $I^{+(-)}$ is the V-LEED scattering intensity measured for the V-LEED target magnetization in the positive (negative) direction. The detailed description of the S-ARPES setup can be found in Ref. [27].

The charge-to-spin conversion is probed by means of longitudinal magneto-optical Kerr effect (L-MOKE). In this case, we used a 691-nm-continuous wave laser as a light source.

The *s*-polarized light was focused on the sample surface with an average polar angle $\vartheta = 45°$, a spot size of diameter 5 μm, and an optical power of $W \approx 125$ μW. The reflected light beam passed through a photoelastic modulator, which modulated the circular polarization of the light at 50 kHz, and a polarizer, before being collected by a photodiode as described in Ref. [28]. We recorded the second harmonic of the signal with a first lock-in amplifier and normalized the result to the sample reflectivity to obtain the pure ellipticity signal. In order to further increase the signal-to-noise ratio, we modulated the charge current at 0.3 Hz and extracted the optical signal with a second lock-in amplifier (for more details about longitudinal MOKE measurements, see Ref. [29] and Sec. E of the Supplemental Material [30]).

To directly probe the spin-to-charge conversion we employ either optical or electrical spin injection. In the first case, a circularly polarized laser beam ($\lambda = 740$ nm) was focused on the sample with a spot-size diameter $s \approx 1.5$ μm and an optical power $W \approx 19$ mW. Optical spin injection generates a spin-oriented population of electrons in the Ge conduction band [31,32], with a spin polarization $P \approx 8\%$ [33,34] parallel to the light wave vector inside Ge [35,36]. Since the experimental geometry is sensitive to the in-plane component of the spin polarization [37], we had the laser beam partially filling off axis a 0.65 numerical aperture objective, focusing the light on the sample with a polar angle $\approx 20°$. The resulting electromotive force is measured under open-circuit conditions [38–40]. The circular polarization is modulated by a photoelastic modulator at 50 kHz and the signal is demodulated by a lock-in amplifier. Furthermore, to increase the signal-to-noise ratio, we also modulate the light intensity at 21 Hz with a chopper, and the signal is extracted by a second lock-in amplifier.

For what concerns electrical spin pumping measurements, a transverse radio frequency field $\mathbf{H}_{rf}$, generated at the center of a cylindrical X-band resonator cavity ($f = 9.7$ GHz, TE$_{011}$ mode), triggers the ferromagnetic resonance of the Co layer and spin pumping. The charge current is given by $I_C = \Delta V/R$, where R is the resistance measured between the two voltage probes [41,42]. To remove the Seebeck contribution to the signal at room temperature, we consider: $I_C = (I_C^{+\mathbf{H}_{dc}} - I_C^{-\mathbf{H}_{dc}})/2$ where $\mathbf{H}_{dc}$ is the DC magnetic field applied in the film plane [43].

III. FILM MORPHOLOGY

As a first step to investigate SCI in Bi-based low-dimensional systems, we analyze the structural and electronic properties of Bi films as a function of the thickness t. To this purpose, we have grown ultrathin Bi films ($t \approx 0$–10 nm) by molecular beam epitaxy (MBE) on a Bi/Ge($\sqrt{3} \times \sqrt{3}$) R 30° wetting layer stabilized on a Ge(111) substrate. The Ge substrate exhibits metallic character in the 30–300 K temperature range. In the following, we call the (110)-oriented films the pseudocubic (PC) phase and (111)-oriented films the hexagonal phase (HEX) by analogy with the Bi/Si(111) system [20]. Structural characteristics of thin Bi films on Ge(111) were investigated by means of several techniques. However, x-ray diffraction (XRD) shows that PC and HEX films exhibit the same bulk rhombohedral crystal structure with the same
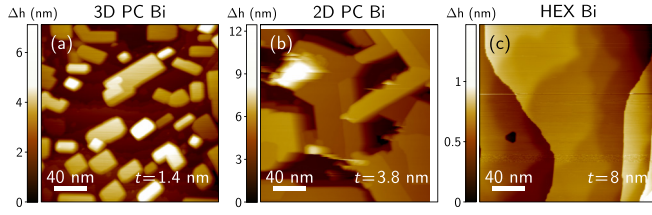
FIG. 1. Morphology of Bi films grown on Ge(111) as a function of the film thickness t. Typical STM images of (a) pseudocubic Bi nanocrystals (3D PC) for $t < 3.5$ nm, (b) percolated pseudocubic Bi nanocrystals forming a 2D layer (2D PC) for $t = 3.8$ nm, and (c) continuous Bi film with (111) orientation for $t = 8$ nm. The thickness t is calculated starting from the Bi/Ge(111)-($\sqrt{3} \times \sqrt{3}$) $R\,30°$ wetting layer.

lattice parameter (for more details about the x-ray diffraction results, see Sec. B of the Supplemental Material [30]). There is no evidence for strain effects in both phases. Hence, the only difference between PC and HEX films is the crystal orientation of the free surface: (110) for the PC phase and (111) for the HEX one. The Bi growth proceeds as shown in Fig. 1 by STM: Up to $t = 3.5$ nm, we observe the formation of isolated three-dimensional PC flat nanocrystals or nanoplatelets [3D PC phase, Fig. 1(a)]; for $3.5 < t < 4$ nm, the PC nanocrystals start percolating to form a 2D layer [2D PC phase, Fig. 1(b)]; for $4 < t < 5$ nm, there is coexistence of the PC and HEX (PC+HEX) phases and above 5 nm we only observe the single crystalline HEX phase [Fig. 1(c)]. This scenario is confirmed by *in situ* reflection high-energy electron diffraction (RHEED) and grazing x-ray diffraction. The RHEED patterns (resp. grazing x-ray diffraction spectra) are shown in Sec. A (resp. Sec. B) of the Supplemental Material [30].

IV. ELECTRONIC PROPERTIES

A. Band structure

The electronic properties of *in situ* grown Bi/Ge(111) samples have been characterized by means of ARPES with spin resolution (S-ARPES) at the APE beamline of the ELETTRA synchrotron radiation facility. In Figs. 2(a)–2(e), the ARPES spectra collected along the $\overline{K}$-$\overline{\Gamma}$-$\overline{M}$ directions of the Ge(111) surface Brillouin zone [SBZ; sketched in the inset of Fig. 2(a)] are reported as a function of the Bi thickness. At the early stages of growth, in the 3D PC regime ($t = 1$–3.5 nm), we observe states crossing the Fermi level (E_F) around the $\overline{\Gamma}$ point with a hole character. In analogy with what Bian *et al.* observed on thin Bi/Si(111) [45], we conclude that these are surface states with a very short spatial extension of only 2 Bi bilayers (1 BL = 3.28 Å), as shown in Fig. 4 of Ref. [45]. In this regime, we do not clearly observe other surface or bulk states close to E_F. For $t = 5$ nm, the band structure has evolved and clearly shows occupied states around $k_\| = 0.7$ Å^{-1} along both the $\overline{\Gamma}$-$\overline{K}$ and $\overline{\Gamma}$-$\overline{M}$ directions. At this thickness, it is worth comparing our experimental data [Fig. 2(g)] with the calculated 2D Fermi surface of Bi(110) [Fig. 2(f)] [7,44]. In the former, we observe a dark ring around $\overline{\Gamma}$ and twelve elongated low-intensity rings centered around $k_\| = 0.7$ Å^{-1}. This Fermi surface can be reproduced by considering the
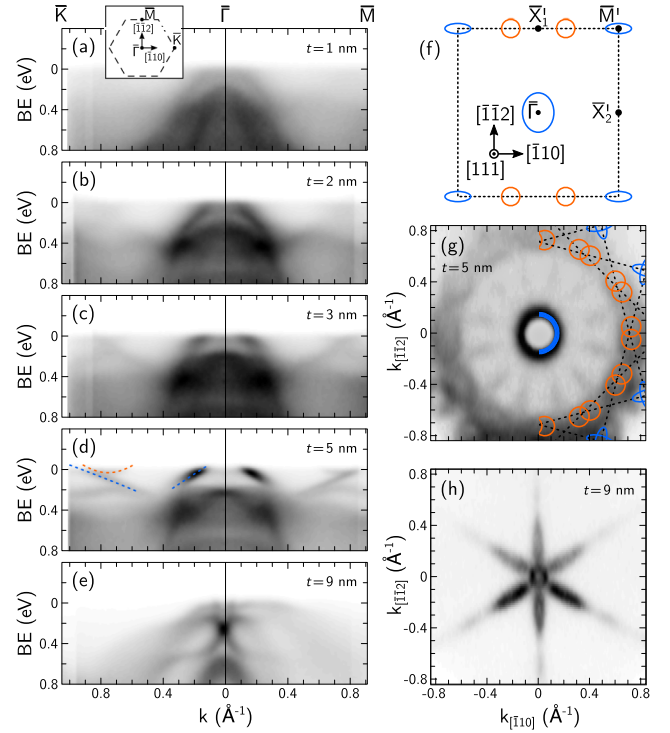

FIG. 2. Thickness evolution of the band structure of Bi/Ge(111) as obtained by ARPES measurements. (a)–(e) Band structure along the $\overline{K}$-$\overline{\Gamma}$-$\overline{M}$ directions for $t = 1$, 2, 3, 5, and 9 nm of Bi deposited on the Bi/Ge(111)-($\sqrt{3} \times \sqrt{3}$) $R\,30°$ wetting layer. $\overline{K}$, $\overline{\Gamma}$, and $\overline{M}$ are high symmetry points of the Ge(111) SBZ shown in the inset of panel (a). BE and k are the electron binding energy and momentum, respectively. Different band structures can be identified depending on the structural phase which are: PC Bi nanocrystals for $t = 1$–3 nm (3D PC phase), a PC Bi film (2D PC phase) for $t = 5$ nm (HEX grains do not give a visible signal), and a (111)-oriented Bi film (HEX phase) for $t = 9$ nm. (f) Schematics of the Bi(110) 2D Fermi surface according to Ref. [44]. $\overline{M}'$, $\overline{\Gamma}' = \overline{\Gamma}$, and $\overline{X_1}'$ and $\overline{X_2}'$ are the high symmetry points of the Bi(110) SBZ. Blue lines (around $\overline{\Gamma}$ and $\overline{M}'$) correspond to hole states while orange ones (near $\overline{X_1}'$) correspond to electron states. They are also reported in (d). $k_{[\bar{1}10]}$, $k_{[\bar{1}\bar{1}2]}$, and $k_{[111]}$ are the basis vectors of the reciprocal space. (g) Experimental 2D Fermi surface for $t = 5$ nm reproduced (in orange and blue lines) by superimposing six times the Fermi surface of bulk Bi(110) in (f). (h) 2D Fermi surface of single crystalline Bi(111) for $t = 9$ nm.

ARPES results of Agergaard *et al.* on the (110) surface of bulk Bi [44] and the first principles calculations of Koroteev *et al.* [7]. Indeed, six equivalent growth orientations of the twofold symmetric Bi(110) surface are detected on the sixfold symmetric Ge(111) surface. For symmetry reasons, there is no preferential orientation of the nanocrystals and the six equivalent orientations are equally populated. The elongated rings correspond to the surface electronic states along the $\overline{M}'$-$\overline{X_1}'$ direction of the Bi(110) SBZ. They are also reported in Fig. 2(d) along with the surface hole states at $\overline{M}'$ which cross the Fermi level at $k_\| = 0.9$ Å^{-1}. Finally, for $t = 9$ nm [Figs. 2(e) and 2(h)], the band structure is the one of single crystalline bulk Bi(111) [46]. We note here that HEX Bi films grow in registry with Ge(111) as shown by the RHEED patterns in Sec. A of the Supplemental Material [30].
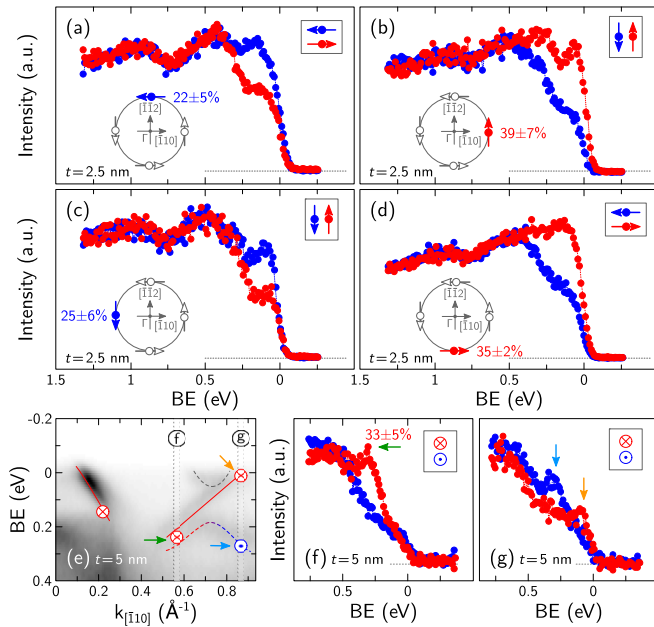
FIG. 3. Spin texture of metallic surface states. (a)–(d) Spin polarization recorded along the $\overline{\Gamma}$ states showing the helical spin texture, for $t = 2.5$ nm. The numbers are the net spin polarization values. (e) Band structure along $\overline{\Gamma}$-$\overline{K}$ for $t = 5$ nm. Red solid lines are $\overline{\Gamma}$ ($k_{[\bar{1}10]} \approx 0.1$ Å^{-1}) and $\overline{M}'$ ($k_{[\bar{1}10]} \approx 0.7$ Å^{-1}) hole states of Bi(110), respectively. Dotted lines crossing the Fermi level correspond to the electron pockets near the $\overline{X_1}'$ point shown in Figs. 2(f) and 2(g). (f),(g) Spin polarization of $\overline{M}'$ states.

B. Spin texture

The results of S-ARPES are shown in Fig. 3. In Figs. 3(a)–3(d), for $t = 2.5$ nm, we probe the surface states around $\overline{\Gamma}$: they exhibit a counterclockwise helical spin texture with a spin polarization P up to 40%. The spin-momentum locking is due to the strong Rashba spin-orbit coupling in the surface states. In Figs. 3(e)–3(g), we show that the states at $\overline{M}'$ for $t = 5$ nm are also spin polarized ($P \approx 30\%$), but they have a clockwise spin helicity, as predicted by Pascual *et al.* [47]. The conclusion of this analysis is that both $\overline{\Gamma}$ and $\overline{M}'$ states can participate to SCI, but they would provide opposite contributions, since they are both holes states and have opposite spin helicities.

V. SCI MEASUREMENTS

A. Charge-to-spin conversion

Based on the accurate knowledge of the atomic and electronic structures of ultrathin Bi films, we then performed SCI measurements as a function of the Bi thickness. Charge-to-spin conversion phenomena can be directly probed by exploiting MOKE. In this respect, the detection of an electrically-induced spin accumulation in metals is particularly challenging, and it has been limited to low temperature ranges [48]. In our case, we exploit longitudinal MOKE [see Fig. 4(a)]: an electrical current flows in 1.5-mm-wide Bi/Ge(111) stripes of constant Bi thickness, and we detect the Kerr rotation signal coming from the Bi film with a double
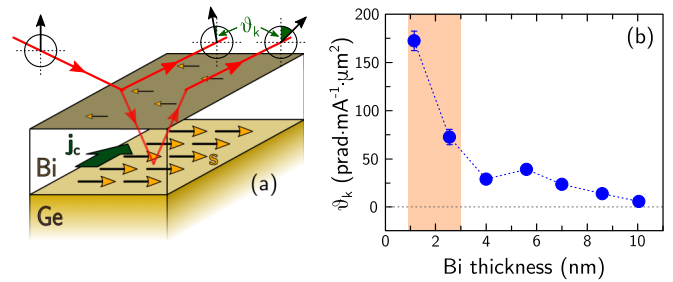

FIG. 4. Charge-to-spin conversion in Bi films probed by MOKE. (a) Schematics of the experimental setup for charge-to-spin conversion. An electrical current flows into or at the surface of the Bi layer and is converted into a spin accumulation at the top and bottom surfaces. The spin accumulation at the bottom surface is detected by longitudinal Kerr effect. (b) Kerr angle ϑ_k detected as a function of the Bi thickness.

modulation technique at room temperature. The details about the longitudinal MOKE measurements are given in Sec. E of the Supplemental Material [30]. As shown in Fig. 4(b), up to $t = 3$ nm we detect a large Kerr signal ϑ_k, which results from the electrically-induced spin accumulation in Bi, whereas ϑ_k rapidly decreases as the Bi thickness is increased.

B. Spin-to-charge conversion

The same qualitative behavior is found when the spin-to-charge conversion generated by a spin current is investigated by either optical spin orientation in Ge [49] or spin pumping from a ferromagnet. Optical spin orientation allows obtaining a spin accumulation with in-plane polarization in Ge by shining circularly polarized light on the sample at a grazing incidence [36]. The spin-polarized electrons then diffuse into the Bi film [Fig. 5(a)] [50]. As an alternative to optical spin orientation, we can also inject a spin current by spin pumping from an Al(5 nm)/Co(15 nm)/Al(3 nm) stack grown on top of Bi at the ferromagnetic resonance of the Co layer [Fig. 5(b)] [51]. In both cases the spin current generates a transverse charge current, which is detected as a voltage ΔV measured between two electrodes deposited across the Bi film in open circuit conditions. The experimental details are given in Sec. F of the Supplemental Material [30]. In Fig. 5(c), we show the results for optical spin orientation measurements: The signal is larger in the 3D PC regime, whereas for $t > 3$ nm, it decreases. Similarly, with spin pumping [Fig. 5(d)] at 30 K and 300 K we observe a sharp decrease of the signal above $t = 3$ nm, with no detectable signal for $t > 4$ nm. The signal at 30 K is roughly one order of magnitude larger compared to that at room temperature. To summarize, in all the SCI experiments we observe a conversion signal for $t < 4$ nm, when Bi nanocrystals are present at the surface of Ge(111), whereas the signal is drastically attenuated for the other morphologies.

VI. DISCUSSION

We can first exclude that the Bi/Ge(111)-($\sqrt{3}\times\sqrt{3}$) R 30° wetting layer significantly contributes to SCI since Aruga *et al.* demonstrated both experimentally and theoretically the absence of spin-polarized states at the Fermi level [52]. The
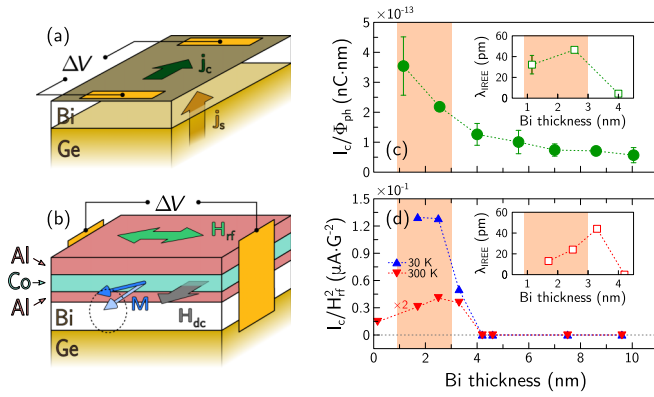
FIG. 5. Spin-to-charge conversion efficiency probed by either optical or electrical spin injection. (a),(b) Schematic drawings showing the experimental geometries used for optical spin orientation and spin pumping measurements, respectively (for more details, see Secs. F and G of the Supplemental Material [30]). (c) Bi-thickness dependence of the spin-to-charge conversion efficiency I_C/Φ_{ph} at room temperature using optical spin orientation. $I_C = \Delta V/R$ is the generated charge current where ΔV is the voltage measured in open circuit conditions upon illumination with circularly polarized light, and R is the electrical resistance between the two contacts estimated using four-probe resistance geometry. The charge current is normalized to the excitation signal, i.e., the photon flux Φ_{ph}. Inset: λ_{IREE} values deduced at room temperature. (d) Bi-thickness dependence of the spin-to-charge conversion efficiency I_C/H_{rf}^2 at 30 K and room temperature using spin pumping. $I_C = \Delta V/R$ is the generated charge current where ΔV is the voltage measured in open circuit conditions at the ferromagnetic resonance of the Co electrode and R is the electrical resistance between the two contacts. The charge current is normalized to the excitation signal, i.e., the radio frequency power proportional to H_{rf}^2. Inset: λ_{IREE} values deduced at room temperature.

SCI signal vanishes when PC nanocrystals start to percolate: The system turns from 3D (or 0D if we consider the nanocrystals as quantum dots) to 2D. This transition occurs in the PC phase and is not related to the transition from the PC to the HEX phase. It is only related to the film morphology. Hence, the interconversion takes place within or at the surface of nanocrystals of a given height h and lateral size $a = \sqrt{S}$, S being the nanocrystal area. STM images show that the lateral size a of nanocrystals is comparable to the Fermi wavelength, and since $h \ll a$, quantum confinement effects play a fundamental role in determining the spin-transport properties of the system. Indeed, due to the low effective mass of electrons in bulk Bi, the spacing between discrete energy levels can be large enough to open a band gap E_g' in Bi nanocrystals [53]. Considering a single crystalline rhombohedral Bi film in vacuum and using the bulk electron and hole effective masses, the calculation of E_g' in Sec. D of the Supplemental Material [30] gives a SMSC transition (i.e., $E_g' \geqslant 0$) for $a \leqslant 50$ nm. In our case, the Bi film is in contact with germanium on one side and with MgO or aluminum on the other side, which probably affects the electronic properties of Bi (band structure, effective masses, and confining potentials). The resulting calculated energy shifts and band gap are thus overestimated and represent upper bounds. In a more realistic picture, QSE

are reducing the density of states at the Fermi level by shifting up the electron states at the L point while shifting down the hole states at the T point. It results in an enhancement of the PC nanocrystals bulk resistivity. For the rest of the discussion, we assume that nanocrystals of thickness $h \geqslant 4$ BL (meaning that opposite surface states do not overlap each other [45]) exhibit a high bulk resistivity for lateral size $a \leqslant 50$ nm and a low bulk resistivity for lateral size $a > 50$ nm. The high (resp. low) bulk resistivity state corresponds to a semiconducting (resp. semimetallic) character of nanocrystals.

From an extensive analysis of STM images in Sec. C of the Supplemental Material [30], for $t < 0.9$ nm, the majority of PC nanocrystals are less than 4 BL thick; the top and bottom surface states overlap and the corresponding SCIs, being of opposite sign, cancel each other. For $0.9 < t < 3$ nm, the nanocrystals have a semiconducting character. The surface states do not overlap and are electrically separated because of the high bulk resistivity. As a consequence, SCI at each interface is allowed and no communication channel between opposite interfaces is present. We can observe a net SCI signal. This thickness range is reported as a shaded area in Figs. 4(b), 5(c), and 5(d), and it nicely fits the thickness range where we experimentally observe a conversion signal. This interpretation is in agreement with the increase of the spin-pumping signal at low temperature. For $0.9 < t < 3$ nm, Bi nanocrystals have a semiconducting character and the number of thermally excited electrons is lower at 30 K than at room temperature, which increases the bulk resistivity. Spin-to-charge conversion takes place at the $\overline{\Gamma}$ states in Figs. 2(a)–2(c) due to their helical spin texture shown in Figs. 3(a)–3(d), thus it can be attributed to the IREE. Concerning Kerr measurements, in this thickness range most of the current flows at the Bi/Ge interface, where the conductivity of the Rashba electron gas is large [54]. As a consequence, the REE generates an in-plane spin accumulation, with a spin polarization perpendicular to the current density vector. We detect a very large Kerr signal [Fig. 4(b)], which is proportional to the electrically-induced spin density at the Bi/Ge interface, since the absorption length α of the incident light ($\alpha = 16$ nm for $\lambda = 691$ nm) is much larger than the nanocrystal height [55]. Finally, for $t > 3$ nm, nanocrystals exhibit lateral sizes larger than λ_F and start percolating. This reduces and finally suppresses quantum confinement at room temperature. In these conditions, spin-polarized electrons diffuse in the entire film thickness, and being $h < l_{sf}$, the spin-to-charge conversions at both interfaces compensate each other reducing the signal down to zero. Similarly, for charge-to-spin conversion, when nanocrystals become more and more conducting, electrical currents flow at both interfaces, causing opposite spin accumulations, which tend to cancel each other. Hence, the Kerr signal drastically decreases. In a simple model, the effect of quantum confinement on SCI experiments is equivalent to the effect of a variable bulk resistance R_B electrically connecting the top and bottom metallic surface states of resistance R_S. Following Ref. [53], for $t < 3$ nm, quantum confinement leads to $R_B \gg R_S$ and surface states are electrically insulated from each other. We can observe SCI signals. On the other hand, for $t > 3$ nm, $R_B \approx R_S$ and the charge currents in the top and bottom surface states are shunted through the bulk reducing and canceling SCI signals.

We could not detect any spin-to-charge conversion by spin pumping for $t = 50$ nm. This is indicative of negligible bulk spin-to-charge conversion by inverse spin Hall effect and a long spin diffusion length $l_{sf} > 50$ nm. Starting from $t = 3$ nm, $\overline{M}'$ surface states at E_F develop at the surface of Bi nanocrystals and films as shown in Fig. 2. They exhibit a hole character and a spin chirality opposite to the one of $\overline{\Gamma}$ states (Fig. 3), thus also contributing to the decrease of conversion signals.

Spin-to-charge measurements allow extracting the figure of merit of the conversion occurring at the interfaces [insets of Figs. 5(c) and 5(d)]. It corresponds to the IREE length $\lambda_{IREE} = j_c^{2D}/j_s$, where j_c^{2D} is the 2D charge current density (in A m^{-1}) generated by the 3D spin current density j_s (in A m^{-2}) [56]. In order to calculate λ_{IREE} from optical spin orientation and spin pumping measurements (all the calculations details are given in Secs. I.1 and I.2 of the Supplemental Material [30]), we assume that the conversion occurs only in PC nanocrystals that fulfill the conditions $h > 4$ BL (surface states do not overlap) and $a \leqslant 50$ nm (nanocrystals exhibit a high bulk resistivity). The fraction of the sample surface corresponding to these nanocrystals is given by the analysis of STM images (see Sec. C of the Supplemental Material [30]). In the conversion process, the transverse charge current generated at the nanocrystal interfaces is transferred to the conducting Ge substrate for optical spin orientation experiments and to the Al/Co/Al metallic trilayer for spin pumping experiments. It is then detected as a voltage in open circuit conditions. We obtain a maximum calculated value of ≈ 50 pm by both optical spin orientation and spin pumping for $t \approx 3$ nm. It shows that the spin-to-charge conversion efficiencies are comparable at the Bi/Ge and Bi/Al interfaces and that SCI occurs into the $\overline{\Gamma}$ surface states of Bi regardless of the material at the interface. It is important to note that such a calculation is performed under the assumption that the bulk resistivity of the nanocrystals is large enough to avoid spin diffusion between the two interfaces. If a lower resistivity value were taken into account, the λ_{IREE} value would be drastically larger, so that 50 pm represents a lower bound estimation of the spin-to-charge interconversion efficiency. This λ_{IREE} value is comparable to the ones obtained at different Rashba interfaces such as Ag/Bi (100–300 pm) [56,57], Ag/Sb (30 pm) [57], or Cu/Bi (9 pm) [13]. For Rashba interfaces, $\lambda_{IREE} = \alpha_R \tau/\hbar$ where α_R is the Rashba coefficient and τ is the momentum relaxation time in the interface states. From Ref. [7], we can estimate $\alpha_R \approx 1.5 \times 10^{-10}$ eV m at the Bi(110) surface assuming nearly free electrons in surface states, which gives $\tau \approx 0.2$ fs. This value is of the same order of magnitude as τ values obtained at other Rashba interfaces [13,56,58].

To summarize, we carried out careful structural and electronic characterizations of Bi thin films epitaxially grown on Ge(111). SCI in Bi layers was investigated by Kerr effect, optical spin orientation, and spin pumping. In all three techniques, a conversion signal was only observed in the $t = 1$–3 nm thickness range corresponding to the presence of Bi(110) nanocrystals. We thus interpreted the results as a consequence of QSE and SCI by (I)REE at the surface of nanocrystals exhibiting a semiconducting character. Eventually, we found a λ_{IREE} value as high as 50 pm at the Bi/Ge interface which shows the potential of this interface to manipulate spin currents in Ge. Our results pave the way for the exploitation of QSE to tune SCI, and open a route to manipulate spin currents in Ge by Rashba effect at the interface with a metal [24].

ACKNOWLEDGMENTS

[1] Y. Fuseya, M. Ogata, and H. Fukuyama, J. Phys. Soc. Jpn. **84**, 012001 (2015).

[2] L. Schubnikov and W. J. de Haas, Proc. R. Neth. Acad. Arts Sci. **33**, 130 (1930).

[3] T. J. Seebeck, Abh. Akad. Wiss. Berlin, 289 (1821).

[4] I. Aguilera, C. Friedrich, and S. Blügel, Phys. Rev. B **91**, 125129 (2015).

[5] P. Hofmann, Prog. Surf. Sci. **81**, 191 (2006).

[6] Y. Ohtsubo, J. Mauchain, J. Faure, E. Papalazarou, M. Marsi, P. Le Fèvre, F. Bertran, A. Taleb-Ibrahimi, and L. Perfetti, Phys. Rev. Lett. **109**, 226404 (2012).

[7] Y. M. Koroteev, G. Bihlmayer, J. E. Gayone, E. V. Chulkov, S. Blügel, P. M. Echenique, and P. Hofmann, Phys. Rev. Lett. **93**, 046403 (2004).

[8] N. Garcia, Y. H. Kao, and M. Strongin, Phys. Rev. B **5**, 2029 (1972).

[9] V. P. Duggal and R. Rup, J. Appl. Phys. **40**, 492 (1969).

[10] Y.-M. Lin, S. B. Cronin, J. Y. Ying, M. S. Dresselhaus, and J. P. Heremans, Appl. Phys. Lett. **76**, 3944 (2000).

[11] Y.-M. Lin, X. Sun, and M. S. Dresselhaus, Phys. Rev. B **62**, 4610 (2000).

[12] H. Emoto, Y. Ando, E. Shikoh, Y. Fuseya, T. Shinjo, and M. Shiraishi, J. Appl. Phys. **115**, 17C507 (2014).

[13] M. Isasa, M. C. Martínez-Velarte, E. Villamor, C. Magén, L. Morellón, J. M. De Teresa, M. R. Ibarra, G. Vignale, E. V. Chulkov, E. E. Krasovskii, L. E. Hueso, and F. Casanova, Phys. Rev. B **93**, 014420 (2016).

[14] H. J. Zhang, S. Yamamoto, B. Gu, H. Li, M. Maekawa, Y. Fukaya, and A. Kawasuso, Phys. Rev. Lett. **114**, 166602 (2015).

[15] S. Sangiao, J. M. De Teresa, L. Morellon, I. Lucas, M. C. Martinez-Velarte, and M. Viret, Appl. Phys. Lett. **106**, 172403 (2015).

[16] H. Emoto, Y. Ando, G. Eguchi, R. Ohshima, E. Shikoh, Y. Fuseya, T. Shinjo, and M. Shiraishi, Phys. Rev. B **93**, 174428 (2016).

[17] D. Hou, Z. Qiu, K. Harii, Y. Kajiwara, K.-c. Uchida, Y. Fujikawa, H. Nakayama, T. Yoshino, T. An, K. Ando, X. Jin, and E. Saitoh, Appl. Phys. Lett. **101**, 042403 (2012).

[18] K.-I. Lee, J. W. Roh, J. Chang, S.-H. Han, K.-H. Shin, W. Y. Jeung, M. Johnson, and W. Lee, Phys. Rev. B **79**, 195201 (2009).

[19] J. Fan and J. Eom, Appl. Phys. Lett. **92**, 142101 (2008).

[20] T. Nagao, J. T. Sadowski, M. Saito, S. Yaginuma, Y. Fujikawa, T. Kogure, T. Ohno, Y. Hasegawa, S. Hasegawa, and T. Sakurai, Phys. Rev. Lett. **93**, 105501 (2004).

[21] S. Ito, B. Feng, M. Arita, A. Takayama, R.-Y. Liu, T. Someya, W.-C. Chen, T. Iimori, H. Namatame, M. Taniguchi, C.-M. Cheng, S.-J. Tang, F. Komori, K. Kobayashi, T.-C. Chiang, and I. Matsuda, Phys. Rev. Lett. **117**, 236402 (2016).

[22] B. Weitzel and H. Micklitz, Phys. Rev. Lett. **66**, 385 (1991).

[23] C. A. Hoffman, J. R. Meyer, F. J. Bartoli, A. Di Venere, X. J. Yi, C. L. Hou, H. C. Wang, J. B. Ketterson, and G. K. Wong, Phys. Rev. B **48**, 11431 (1993).

[24] S. Oyarzún, A. K. Nandy, F. Rortais, J.-C. Rojas-Sánchez, M.-T. Dau, P. Noël, P. Laczkowski, S. Pouget, H. Okuno, L. Vila, C. Vergnaud, C. Beigné, A. Marty, J.-P. Attané, S. Gambarelli, J.-M. George, H. Jaffrès, S. Blügel, and M. Jamet, Nat. Commun. **7**, 13857 (2016).

[25] S. Hatta, Y. Ohtsubo, S. Miyamoto, H. Okuyama, and T. Aruga, Appl. Surf. Sci. **256**, 1252 (2009).

[26] F. Bottegoni, A. Calloni, G. Bussetti, A. Camera, C. Zucchetti, M. Finazzi, L. Duò, and F. Ciccacci, J. Phys.: Condens. Matter **28**, 195001 (2016).

[27] C. Bigi, P. K. Das, D. Benedetti, F. Salvador, D. Krizmancic, R. Sergo, A. Martin, G. Panaccione, G. Rossi, J. Fujii, and I. Vobornik, J. Synchrotron Radiat. **24**, 750 (2017).

[28] Z. J. Yang and M. R. Scheinfein, J. Appl. Phys. **74**, 6810 (1993).

[29] F. Bottegoni, C. Zucchetti, S. Dal Conte, J. Frigerio, E. Carpene, C. Vergnaud, M. Jamet, G. Isella, F. Ciccacci, G. Cerullo, and M. Finazzi, Phys. Rev. Lett. **118**, 167402 (2017).

[30] See Supplemental Material at http://link.aps.org/supplemental/10.1103/PhysRevB.98.184418 for details about the MBE growth and RHEED patterns (Sec. A), x-ray diffraction (Sec. B), the analysis of STM images (Sec. C), quantum size effects calculations (Sec. D), longitudinal MOKE (Sec. E), optical spin orientation (Sec. F), spin pumping-FMR (Sec. G), and the estimation of IREE length by optical (Sec. I.1) and electrical (Sec. I.2) spin injection.

[31] F. Bottegoni, A. Ferrari, F. Rortais, C. Vergnaud, A. Marty, G. Isella, M. Finazzi, M. Jamet, and F. Ciccacci, Phys. Rev. B **92**, 214403 (2015).

[32] C. Zucchetti, F. Bottegoni, G. Isella, M. Finazzi, F. Rortais, C. Vergnaud, J. Widiez, M. Jamet, and F. Ciccacci, Phys. Rev. B **97**, 125203 (2018).

[33] A. Giorgioni, E. Vitiello, E. Grilli, M. Guzzi, and F. Pezzoli, Appl. Phys. Lett. **105**, 152404 (2014).

[34] J. Rioux and J. E. Sipe, Phys. Rev. B **81**, 155215 (2010).

[35] F. Meier and B. Zakharchenya, *Optical Orientation (Modern Problems in Condensed Matter Sciences)*, Vol. 8 (Elsevier, Amsterdam, 1984).

[36] D. T. Pierce and F. Meier, Phys. Rev. B **13**, 5484 (1976).

[37] F. Bottegoni, C. Zucchetti, F. Ciccacci, M. Finazzi, and G. Isella, Appl. Phys. Lett. **110**, 042403 (2017).

[38] M. I. Dyakonov and A. Khaetskii, *Spin Physics in Semiconductors* (Springer, Berlin, 2008), pp. 211–243.

[39] K. Ando, M. Morikawa, T. Trypiniotis, Y. Fujikawa, C. H. W. Barnes, and E. Saitoh, J. Appl. Phys. **107**, 113902 (2010).

[40] C. Zucchetti, F. Bottegoni, C. Vergnaud, F. Ciccacci, G. Isella, L. Ghirardini, M. Celebrano, F. Rortais, A. Ferrari, A. Marty, M. Finazzi, and M. Jamet, Phys. Rev. B **96**, 014403 (2017).

[41] S. Gupta, R. Medwal, D. Kodama, K. Kondou, Y. Otani, and Y. Fukuma, Appl. Phys. Lett. **110**, 022404 (2017).

[42] Y. Tserkovnyak, A. Brataas, G. E. W. Bauer, and B. I. Halperin, Rev. Mod. Phys. **77**, 1375 (2005).

[43] Y. Shiomi, K. Nomura, Y. Kajiwara, K. Eto, M. Novak, K. Segawa, Y. Ando, and E. Saitoh, Phys. Rev. Lett. **113**, 196601 (2014).

[44] S. Agergaard, C. Søndergaard, H. Li, M. B. Nielsen, S. V. Hoffmann, Z. Li, and P. Hofmann, New J. Phys. **3**, 15 (2001).

[45] G. Bian, T. Miller, and T.-C. Chiang, Phys. Rev. B **80**, 245407 (2009).

[46] T. Hirahara, T. Nagao, I. Matsuda, G. Bihlmayer, E. V. Chulkov, Y. M. Koroteev, P. M. Echenique, M. Saito, and S. Hasegawa, Phys. Rev. Lett. **97**, 146803 (2006).

[47] J. I. Pascual, G. Bihlmayer, Y. M. Koroteev, H.-P. Rust, G. Ceballos, M. Hansmann, K. Horn, E. V. Chulkov, S. Blügel, P. M. Echenique, and P. Hofmann, Phys. Rev. Lett. **93**, 196802 (2004).

[48] C. Stamm, C. Murer, M. Berritta, J. Feng, M. Gabureac, P. M. Oppeneer, and P. Gambardella, Phys. Rev. Lett. **119**, 087203 (2017).

[49] F. Bottegoni, M. Celebrano, M. Bollani, P. Biagioni, G. Isella, F. Ciccacci, and M. Finazzi, Nat. Mater. **13**, 790 (2014).

[50] G. Isella, F. Bottegoni, A. Ferrari, M. Finazzi, and F. Ciccacci, Appl. Phys. Lett. **106**, 232402 (2015).

[51] K. Ando, S. Takahashi, J. Ieda, Y. Kajiwara, H. Nakayama, T. Yoshino, K. Harii, Y. Fujikawa, M. Matsuo, S. Maekawa, and E. Saitoh, J. Appl. Phys. **109**, 103913 (2011).

[52] T. Aruga, J. Electron Spectrosc. Relat. Phenom. **201**, 74 (2015).

[53] Z. B. Zhang, X. Sun, M. S. Dresselhaus, J. Y. Ying, and J. Heremans, Phys. Rev. B **61**, 4850 (2000).

[54] J. Sinova, S. O. Valenzuela, J. Wunderlich, C. Back, and T. Jungwirth, Rev. Mod. Phys. **87**, 1213 (2015).

[55] H.-J. Hagemann, W. Gudat, and C. Kunz, J. Opt. Soc. Am. **65**, 742 (1975).

[56] J. C. Rojas-Sánchez, L. Vila, G. Desfonds, S. Gambarelli, J. P. Attané, J. M. De Teresa, C. Magén, and A. Fert, Nat. Commun. **4**, 2944 (2013).

[57] W. Zhang, M. B. Jungfleisch, W. Jiang, J. E. Pearson, and A. Hoffmann, J. Appl. Phys. **117**, 17C727 (2015).

[58] K. Shen, G. Vignale, and R. Raimondi, Phys. Rev. Lett. **112**, 096601 (2014).